Journal of Materials Chemistry A

ROYAL SOCIETY OF CHEMISTRY

PAPER

View Article Online
View Journal

Cite this: DOI: 10.1039/d5ta09966h

Fast hydride-ion conduction in complex hydride Ba_2MgH_6

Nur Ika Puji Ayu, [ab] Naoki Matsui,*[c] Yoshitake Toda, [d] Takeya Mezaki,[d] Guangzhong Jiang,[b] Kota Suzuki[ce] and Ryoji Kanno*[c]

Received 5th December 2025
Accepted 23rd March 2026

DOI: 10.1039/d5ta09966h

rsc.li/materials-a

Hydride-ion conductors are required to design hydride-based electrochemical devices for energy conversion and storage. However, developing a hydride-ion conductor with rapid conduction is challenging and has not been explored thoroughly because of the scarcity of hydride materials exhibiting superionic conductivity. In this study, we employed the complex hydride Ba_2MgH_6 as a hydride-ion conductor, which exhibited a superionic conductivity of 0.125 S cm^{-1} at 693 K. The superionic state was induced by the formation of the Schottky charge-neutral defect pair of one Ba and two H atoms while maintaining the structural framework. The hydrogen vacancies created at temperatures >625 K facilitated rapid hydride-ion conduction. Density functional theory-based molecular dynamics simulations revealed that defect-free Ba_2MgH_6 does not show hydride-ion conduction, whereas the defective $Ba_{2-\delta}MgH_{6-2\delta}$ (δ = 0.125) shows rapid hydride-ion conduction along its c-axis. We believe that this superionic conduction in Ba_2MgH_6 induced by Schottky defects will enable the design of superionic hydride-ion conductors *via* defect engineering.

Introduction

Ionic conductors can be used as solid electrolytes for electrochemical devices. To date, Li^+, Na^+, H^+, F^-, and O^{2-} ionic conductors have been developed as solid electrolyte materials for all-solid-state batteries and solid oxide fuel cells. A hydride ion (H^-) is an emerging alternative charge carrier owing to its large polarizability and optimal ionic radius (1.27–1.52 Å),[1] which enables high conductivity. Therefore, hydride-ion-driven electrochemical devices are desirable and have significant potential. Thus far, various hydride-ion conductors with diverse crystal structures have been developed to achieve high hydride-ion conductivity. These include cotunnite-type BaH_2,[2] K_2NiF_4-type such as $Ln_{2-x-y}Ae_{x+y}LiH_{1-x+y}O_{3-y}$ (Ln = La–Gd, Ae = Sr, Ba)[3–5] and Ba_2MHO_3 (M = Sc, Y),[6,7] anti-CdI_2-type Ba_2H_3X (X = Cl, Br, I),[8] anti-α-AgI–type $Ba_{0.5}Ca_{0.35}Na_{0.15}H_{1.85}$,[9] fluorite-type $LnH_{3-2x}O_x$ and LaH_x,[10–12] and perovskite-type hydrides such as $Sr_{0.925}Na_{0.075}LiH_{2.925}$ and the $SrLiH_3$–$CaLiH_3$–$NaLiH_2$ system.[13,14] In all these diverse structures, a hydrogen vacancy or interstitial hydrogen exists in the anion sublattice, which facilitates hydride-ion conduction.

Perovskite-type structures are among the most common structural frameworks used for hydride-ion conductors. In the simple perovskite (ABX_3) structure, BX_6 octahedra are connected by corner-sharing to form a three-dimensional network. These interconnected octahedra provide a long-range conduction pathway for the anions; $Sr_{0.925}Na_{0.075}LiH_{2.925}$ shows a high hydride-ion conductivity of 5.0 × 10^{-6} S cm^{-1}.[13] Varying the connectivity of the BX_6 unit results in diverse derivatives. For example, the BX_6 octahedra in the K_2NiF_4-type structure are connected in two dimensions to form perovskite layers, which are structurally disconnected by rock-salt-type interlayers. The K_2NiF_4-type structure offers an alternative conduction pathway across the disconnected interlayer. Therefore, a hydride-ion conductor can be designed in frameworks with disconnected polyhedra. Similar challenges have been encountered in fluoride-ion conductors, which share structural analogies with hydride-ion conductors and are being explored for all-solid-state fluoride-ion batteries.[15] The limited variety of known structure types, such as fluorite, perovskite, and tysonite, hinders further enhancement of F^- conductivity, necessitating the exploration of new structural frameworks. Recent advances in tailoring the polyhedral units of perovskite- and fluorite-type structures have expanded the material space of F^- conductors,[16,17] and such strategies could be extended to H^- conductors.

[a]Department of Physics, Universitas Indonesia, Depok 16424, Indonesia
[b]Research Center for All-Solid-State Battery, Institute of Innovation Research, Tokyo Institute of Technology, 4259 Nagatsuta-cho, Midori-ku, Yokohama 226-8501, Japan
[c]Research Center for All-Solid-State Battery, Institute of Integrated Research, Institute of Science Tokyo, 4259 Nagatsuta-cho, Midori-ku, Yokohama, Kanagawa 226-8501, Japan. E-mail: matsui.n.ee49@m.isct.ac.jp; kanno.r.ade9@m.isct.ac.jp
[d]AGC Inc., Yokohama Technical Center, 1-1, Suehiro-cho, Tsurumi-ku, Yokohama-shi, Kanagawa 230-0045, Japan
[e]Department of Chemical Science and Engineering, School of Materials and Chemical Technology, Institute of Science Tokyo, 4259 Nagatsuta-cho, Midori-ku, Yokohama, Kanagawa 226-8501, Japan

Complex hydrides with isolated MH_n polyhedra acting as a polyanion framework have been widely studied as cation conductors, but rarely studied as hydride-ion conductors, except for $Sr_{1-y}Na_yLiH_{3-x-y}(BH_4)_x$ thus far.[18] In this study, we explored hydride-ion conduction in the cryptohalite-type complex hydride Ba_2MgH_6 containing isolated $(MgH_6)^{4-}$ octahedra. Ba_2MgH_6 has a hexagonal structure with a Ba–MgH_6–Ba layer. Ba is coordinated by twelve hydrogens. We synthesized Ba_2MgH_6 under high pressure, and the hydride-ion conductivity was measured using alternating current (AC) electrochemical impedance spectroscopy (EIS) and isotope-exchange studies. Furthermore, high-temperature X-ray diffraction measurements and first-principles calculations were performed to elucidate the conduction mechanism.

Experimental

Ba_2MgH_6 was prepared by both high-pressure and mechanochemical synthesis. For the high-pressure synthesis, stoichiometric amounts of BaH_2 (95.8%, Mitsuwa, Japan) and MgH_2 (>99%, Mitsuwa, Japan) in a molar ratio of 2 : 1 were mixed by planetary ball milling (Fritsch, P-7, Germany) at 300 rpm for 3 h in a sealed ZrO_2 pot with ZrO_2 balls of 10 mm diameter. The mixed powder was compressed into pellets of 4 mm diameter. The sample pellets were assembled into a pyrophyllite cell consisting of a graphite heater, NaCl, and a BN sleeve. A mixture of $NaBH_4$ and $Ca(OH)_2$ was placed in the cell as the hydrogen source and separated from the sample using BN partition.[5] The pyrophyllite cell was pressed using a cubic anvil up to a pressure of 5 GPa, sintered at 1173 K for 30 min, and quenched to room temperature, following which the pressure was gradually released. The synthesized samples were handled in an Ar-filled glovebox. An off-white product was obtained and subjected to X-ray diffraction (XRD) with Cu Kα radiation (Rigaku, MiniFlex600, Japan) for phase identification. For comparison, Ba_2MgH_6 was also synthesized by the mechanochemical reaction from the same starting materials using planetary ball milling at 600 rpm for 12 h under an Ar atmosphere.

The ionic conductivity was determined by EIS using a frequency response analyser (Biologic, VSP-300, France) in the range of 7 MHz–0.5 Hz with an applied amplitude of 50 mV. For the high-pressure sample, the pellet was placed between Au electrodes of 2 mm thickness and mounted in a gas-tight electrochemical measurement cell (ProboStat, NORECs, Norway). The temperature-dependent conductivity of the sample was evaluated in the range of 349–704 K under an H_2 gas flow of 50 mL min^{-1}. Direct current (DC) measurement was performed at 661 K at an applied voltage of 0.05–0.2 V. Deuterium (D_2) exchange measurement was performed by treating the pellet sample of Ba_2MgH_6 in a ProboStat at 661 K under a flow of D_2 (50 mL min^{-1}) for approximately 1 h while continuously recording EIS data. After observing a relatively stable conductivity, the gas flow was switched to H_2 (50 mL min^{-1}). For the mechanochemically synthesized sample, the obtained powders were cold-pressed at 340 MPa into a pellet (10 mm diameter; 0.7 mm thickness). Gold powder was applied on both sides as current collectors. Conductivity measurements were performed from room temperature to 473 K under vacuum.

The temperature-dependent synchrotron X-ray diffraction (SXRD) data were collected at BL02B2, SPring-8.[19] The sample was vacuum-sealed inside a quartz capillary of 0.3 mm diameter. Diffraction data were collected from 300 K to 773 K in the 2θ range of 2–78° with a fixed wavelength of 0.499403(1) Å. The obtained SXRD data were analyzed using Z-Rietveld software,[20,21] and the crystal structure was drawn using VESTA.[22]

First-principles density functional theory (DFT) calculations were conducted using the projector augmented wave method,[23,24] and the PBEsol functional[25] as executed in the VASP code.[26–28] For the computations with and without lattice parameter relaxation, the plane-wave cut-off energies of 520 and 400 eV were used. The computational lattice parameters were derived by completely relaxing the lattice parameters and internal coordinates. The convergence threshold for self-consistency was 10^{-6} eV for all calculations. Nudged elastic band (NEB) calculations were performed using a 2 × 2 × 2 supercell with a 2 × 2 × 2 Monkhorst–Pack *k*-mesh. A Schottky defect was generated by removing one Ba and two neighbouring H atoms from the supercell. The DFT-molecular dynamics (DFT-MD) simulation was performed on the defective cells. The simulation was performed for 50 ps with a time step of 0.5 fs in the *NVT* ensemble with the Nosé–Hoover thermostat.[29] A 2 × 2 × 2 supercell with a 1 × 1 × 1 single gamma-centred *k*-point was used for the DFT-MD simulations. The probability density of hydrogen was evaluated using the program in the pymatgen-diffusion-package.[30,31]

Results and discussion

Fig. 1 shows the refined SXRD pattern of Ba_2MgH_6 prepared by high-pressure synthesis. Ba_2MgH_6 crystallized in a trigonal $P\bar{3}m1$ space group. The lattice parameters of Ba_2MgH_6 (a = 5.73090(1) Å and c = 4.518670(3) Å) are similar to those previously reported (a = 5.7257(7) Å and c = 4.5148(9) Å).[32] The

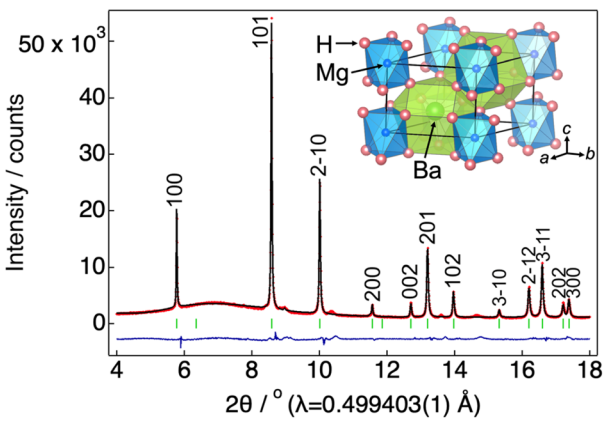

Fig. 1 SXRD pattern of Ba_2MgH_6 at 300 K. The black, red, and blue lines represent calculated, observed, and difference profiles, respectively. The green marks represent the peak positions of Ba_2MgH_6.[32] The inset shows the crystal structure with Ba, Mg, and H depicted in green, blue, and pink, respectively.

refined structure parameters of Ba_2MgH_6 determined from SXRD analysis at 298 K are summarized in Table S1. In this structure, each Mg^{2+} is coordinated by six H^- ions, forming isolated MgH_6 octahedra aligned parallel to the *c*-axis. Ba^{2+} are coordinated by twelve H^- ions, forming BaH_{12} cuboctahedra that share three corners and three faces with six equivalent MgH_6 octahedra and faces with eight equivalent BaH_{12} cuboctahedra.

Fig. 2(a) displays a Nyquist plot of Ba_2MgH_6. At low temperatures such as 614 K, the total ionic conductivity of Ba_2MgH_6 was determined from the sum of the bulk and grain-boundary resistances obtained from the semicircle. At high temperatures such as 662 K, a spike originating from the capacitive electrode interface was observed, and the total conductivity was determined from the real-axis intercept. Fig. 2(b) shows the Arrhenius plot of Ba_2MgH_6, which indicates a relatively low conductivity (2.6×10^{-7} S cm^{-1}) at 477 K with a high activation energy of 91(1) kJ mol^{-1}. This activation energy is two times that of BaH_2 (50 kJ mol^{-1}) but comparable to those reported for $LaH_{3-2x}O_x$ (116–125 kJ mol^{-1}) and $La_{0.6}Sr_{1.4}LiH_{1.6}O_2$ (95 kJ mol^{-1}).[2,4,10] A conductivity jump to 0.125 S cm^{-1} was observed from 635 to 693 K, which is higher than that of

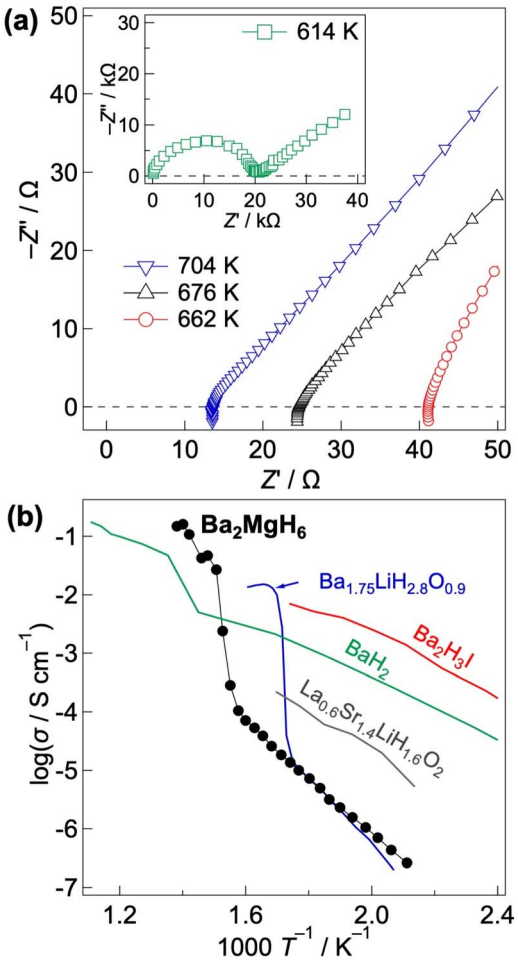

Fig. 2 (a) Nyquist plot of Ba_2MgH_6 at 477–704 K measured under H_2 gas flow and (b) Arrhenius plots of Ba_2MgH_6 (black) and several reported hydride-ion conductors.[2,4,8,33]

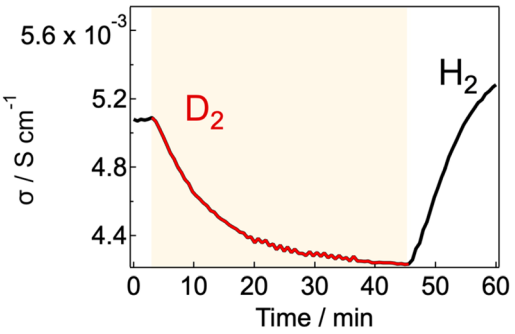

Fig. 3 Conductivity of Ba_2MgH_6 during H/D exchange at 661 K. The black and red lines represent the conductivities measured under H_2 and D_2 gas flow, respectively.

BaH_2 (6×10^{-3} S cm^{-1}).[2] Such changes in conductivity were also observed in other hydride-ion conductors such as BaH_2 and Ba_2LiH_3O, in which structural transitions to higher-symmetry phases have been reported to induce abrupt increases in ionic conductivity.[2,33] The electronic conductivity obtained from the DC measurement at 661 K was 1.1×10^{-3} S cm^{-1} (Fig. S1), whereas the AC conductivity reached 1.3×10^{-2} S cm^{-1}, resulting in an ion transport number of 0.91. Although the high reactivity of H^- with Au current collectors makes the precise estimation of electronic conductivity difficult,[13] the transport number indicates that the major conduction species are hydride ions. It should be noted that the non-ideal capacitive response at low frequencies suggests a contribution from electrode reactions. Separating intrinsic electronic conduction from the H^-/Au interfacial response remains challenging at present. Hydride-ion conduction in Ba_2MgH_6 was further confirmed by H/D isotope exchange. Fig. 3 shows the conductivity of Ba_2MgH_6 at 661 K measured during H/D exchange. Under H_2 gas flow, the conductivity was 5.1×10^{-3} S cm^{-1}, whereas after the H_2 was substituted by D_2, the conductivity decreased to a stable value of 4.2×10^{-3} S cm^{-1}. The isotope effect, defined as σ_H/σ_D, was found to be in the range of 1.20–1.36. This magnitude is consistent with previous reports, in which the classical theory approach attributes the isotope effect primarily to the mass difference between H and D.[34,35] The expected isotope effect in Ba_2MgH_6 is $\sigma_H/\sigma_D = \sqrt{m_D/m_H} = 1.41$, which is comparable to the experimental value. Therefore, the isotope effect demonstrates that conductivity depends strongly on the migrating species (H^- or D^-), providing evidence of hydride-ion conduction in Ba_2MgH_6. The H/D exchange indicates that hydride ions in Ba_2MgH_6 readily exchange with the surrounding gas phase, suggesting that hydrogen evolution may occur in solid-state devices depending on the H_2 partial pressure. Managing such a gas–solid equilibrium would be a key challenge for battery applications, while this facile H_2 exchange also suggests potential applicability to hydrogen storage and release devices.

Temperature-dependent SXRD was performed to examine the structural changes in Ba_2MgH_6 associated with the conductivity jump. Fig. 4(a) shows the temperature-dependent SXRD patterns of Ba_2MgH_6 at 300–773 K. Above 600 K, the diffraction peak intensity of the BaH_2 impurity increases,

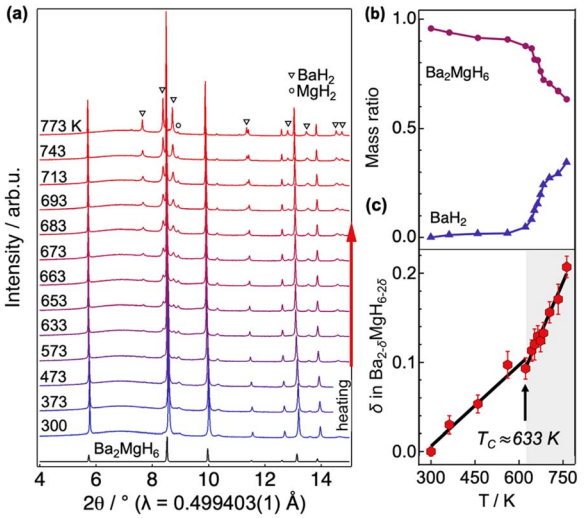

Fig. 4 (a) Temperature-dependent SXRD patterns of Ba_2MgH_6 measured between 300 and 773 K. The triangular and circular markers denote the peak positions of the BaH_2 and MgH_2 impurity phases, respectively. (b) Refined phase fractions of Ba_2MgH_6 (purple circles) and BaH_2 (blue triangle) upon heating. (c) Temperature dependence of Ba vacancies corresponding to the Schottky defect formation in $Ba_{2-\delta}MgH_{6-2\delta}$, which increases significantly above the transition temperature, $T_c \approx 633$ K.

whereas the main phase of Ba_2MgH_6 persists. A minor MgH_2 phase (2–4%) was present from room temperature and remained constant during heating. Fig. 4(b) presents the refined phase fraction of the main phase of Ba_2MgH_6 and BaH_2, indicating a gradual increase in BaH_2 content above 600 K. The Rietveld refinement of Ba_2MgH_6 at each temperature point revealed the presence of barium vacancies, which increased above 633 K. Fig. 4(c) presents the temperature-dependent evolution of the barium vacancies in $Ba_{2-\delta}MgH_{6-2\delta}$. Refined phase fractions and fitting parameters are listed in Table S2. At 773 K, the refined composition was $Ba_{1.78}MgH_{5.56}$ ($\delta = 0.22$, 11% vacancy at the Ba site). The simultaneous formation of BaH_2 impurities and barium vacancies in $Ba_{1.78}MgH_{5.56}$ suggests that BaH_2 was excluded from Ba_2MgH_6 to form non-stoichiometric $Ba_{2-\delta}MgH_{6-2\delta}$. Notably, the onset of the vacancy formation (633–635 K) coincides with the temperature range where the conductivity jump occurred, indicating a correlation between defect generation and superionic conduction.

To elucidate the mechanism of hydride-ion conduction in Ba_2MgH_6, DFT calculations were performed. Fig. S2 shows the calculated electronic density of states (DOS) of Ba_2MgH_6, in which its valence and conduction bands were mainly composed of the H 1s and Ba 5d orbitals, respectively. The occupied H 1s orbital confirms that the hydrogen species behaves as a hydride anion (H^-) rather than an atomic hydrogen (H^0) or proton (H^+). The calculated band gap of 2.7 eV indicates that Ba_2MgH_6 has electronic-insulating character, consistent with its observed ionic conduction behaviour. The effect of the barium and hydrogen vacancies on the ionic conductivity was verified using DFT-MD simulations. The experimentally determined composition $Ba_{1.78}MgH_{5.56}$ was approximated as $Ba_{1.875}MgH_{5.75}$ (15× Ba, 8× Mg, 46× H) in a 2 × 2 × 2 supercell by introducing one Ba and two H vacancies, which represents the closest achievable composition within the supercell constraints. Among twelve possible configurations of one Ba and two H vacancy pairs in the supercell, the most stable structure with the lowest relative energy was selected for the DFT-MD simulations (Fig. S3 and Table S3).

The mean square displacement (MSD) of hydrogen in the stoichiometric structure is shown in Fig. 5(a), and remains nearly zero at all simulated temperatures, indicating hydrogen immobility. Fig. 5(b) demonstrates that the introduction of a pair of Schottky defects results in a significant hydrogen MSD of 34 $Å^2$ at 50 ps and 1000 K, indicating long-range diffusion of hydrogen. The comparison between the calculated conductivity from the MD simulation of the non-stoichiometric model and the experimental results is shown in Fig. 5(c). The conductivity obtained from MD simulation at 725 K was 0.31 S cm^{-1}, comparable to the experimental value (0.16 S cm^{-1}) at 714 K. These results indicate that the high conductivity of Ba_2MgH_6 was attributed to a non-stoichiometric structure containing Schottky defects. The formation of such defects induced superionic behaviour with a calculated formation energy of 0.314 eV per formula unit. According to the Boltzmann distribution, the defect concentration increases with temperature, indicating that $Ba_{2-\delta}MgH_{6-2\delta}$ becomes populated above 600 K (Fig. S4).

Fig. 6 shows the probability density distribution of hydrogen from the MD simulations. In stoichiometric Ba_2MgH_6, no percolation is observed between hydrogen sites as shown in Fig. 6(a). In contrast, in the non-stoichiometric $Ba_{1.875}MgH_{5.75}$ (Fig. 6(b)), hydrogen percolation was observed along the *c*-axis, indicating that the Schottky defect induces hydrogen diffusion predominantly along this direction.

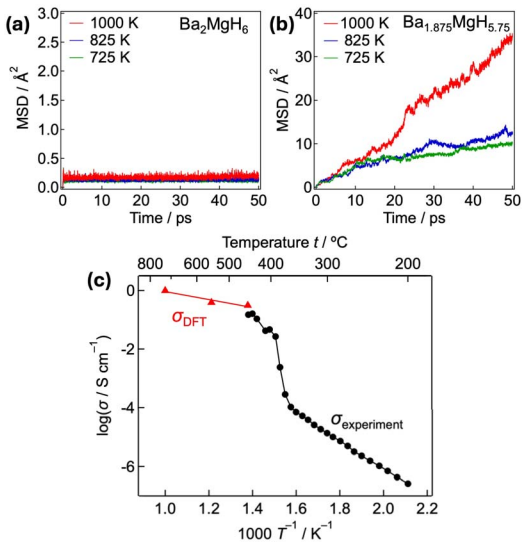

Fig. 5 Mean square displacement (MSD) of hydrogen obtained from molecular dynamics (MD) simulation at 725–1000 K for (a) stoichiometric Ba_2MgH_6 and (b) non-stoichiometric $Ba_{1.875}MgH_{5.75}$. (c) Arrhenius plot of the conductivity of the simulated non-stoichiometric $Ba_{1.875}MgH_{5.75}$ (red triangle) and experimental value (black circle).

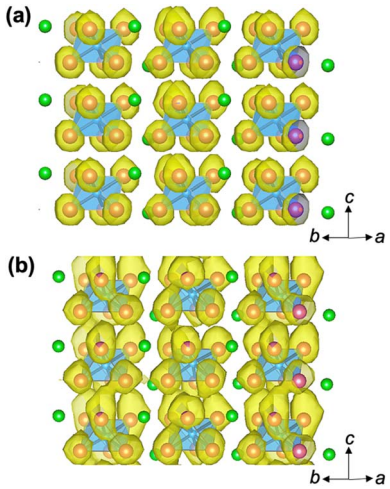

Fig. 6 Probability density distribution of hydrogen for (a) stoichiometric Ba_2MgH_6 and (b) non-stoichiometric $Ba_{1.875}MgH_{5.75}$, obtained from MD simulation. The isosurface level of 5×10^{-4} Å^{-3} is depicted in yellow. The green, blue, and pink spheres represent Ba, Mg, and H, respectively, while the blue octahedra represent the MgH_6 unit.

NEB calculations were performed to clarify the H^- migration process and the associated energy landscape along the intra- and inter-MgH_6 octahedral pathways. Four distinct migration pathways for H^- migration to the nearest neighbour sites are illustrated in Fig. 7(a). These migration pathways can be classified into intra- and inter-octahedral within MgH_6, which are further distinguished by anisotropic migration along the *c*-axis or within the *ab*-plane. Fig. 7(b) presents the migration energy landscape for each pathway, and its corresponding migration barriers are listed in Table 1. The lowest migration barriers were obtained for the hydrogen migration along the *c*-axis *via* inter- and intra-octahedra with migration barriers of 0.13 and 0.34 eV, respectively. The migration along the *ab*-plane demonstrates

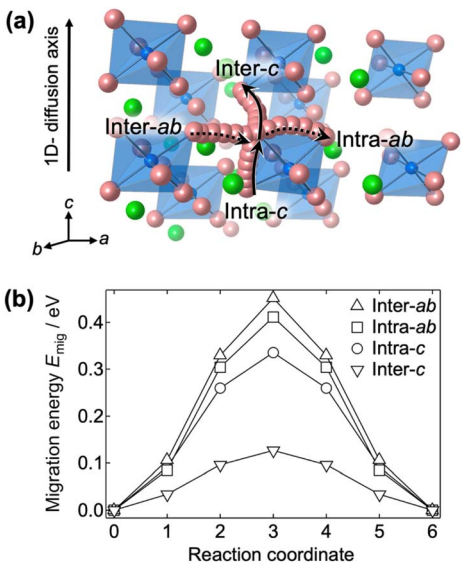

Fig. 7 (a) Schematic illustration of the hydrogen migration pathways *via* hydrogen vacancies to the nearest neighbouring site. (b) Calculated migration energy profiles for each pathway.

Table 1 Migration energies for hydrogen migration *via* hydrogen vacancies to the nearest neighbouring hydrogen sites in Ba_2MgH_6

Migration pathway	Direction	Migration barrier (eV)
Inter-octahedral hopping	*c*-axis	0.13
Intra-octahedral rotation	*c*-axis	0.34
Inter-octahedral hopping	*ab*-plane	0.45
Intra-octahedral rotation	*ab*-plane	0.41

relatively high energy barriers of 0.41 and 0.45 eV for inter- and intra-octahedral, indicating that conduction along this direction is less favourable.

Both the MD and NEB results reveal long-range one-dimensional hydrogen diffusion along the *c*-axis through hydrogen vacancies, involving both inter- and intra-octahedral pathways. A previous study on a proton-conducting oxide material suggested that intra-polyhedral hopping was less likely than inter-polyhedral hopping in the tetrahedral unit.[36] The migration energy landscape is governed by the surrounding atoms and the distance between the initial and final hydrogen positions. The migration barrier along the *ab*-plane is relatively high compared to that along the *c*-axis, owing to the longer H–H distance and the smaller critical radius of the migration pathway formed by three Ba atoms, which results in a relatively strong repulsion between the cations and the moving hydride ions.

Finally, extrinsic defect engineering was employed to enhance the ionic conductivity of Ba_2MgH_6 at moderate temperatures. We attempted aliovalent substitution of Li at the Mg site and K at the Ba site under high-pressure conditions; however, these substitutions did not improve the conductivity due to the poor solubility of the dopants in the Ba_2MgH_6 lattice under high pressure. As an alternative approach to introduce defects, we performed mechanochemical synthesis. Fig. S5 shows the XRD pattern of the mechanochemically synthesized Ba_2MgH_6, confirming that the Ba_2MgH_6 phase was obtained, although the diffraction peaks were notably broadened. The Nyquist plot of the mechanochemical sample (hereafter BM-Ba_2MgH_6) exhibited a clear semicircle in the high-frequency region (Fig. S6). The total conductivity, comprising bulk and grain-boundary contributions, was determined from the resistance of the semicircle. Fig. 8(a) shows the Arrhenius plot of BM-Ba_2MgH_6. At 473 K, the mechanochemically prepared sample exhibited twice the conductivity and half the activation energy of the high-pressure synthesized sample. This indicates that ball milling not only enhances the conductivity of Ba_2MgH_6 but also reduces the migration energy. In a previous study, mechanochemical milling was shown to increase the number of defects and Na^+ conductivity in Na_3PS_4.[37] Optimizing the milling conditions may further enhance the conductivity, although the nature of the defects introduced by mechanochemical synthesis still requires further investigation. Fig. 8(b) shows a comparison of the typical hydride-ion conductors.[2,8,9,11–15,38,39] At elevated temperatures, Ba_2MgH_6 exhibits the highest ionic conductivity among the compared materials, suggesting that the cryptohalite-type structure serves as an intrinsically favourable framework for achieving high

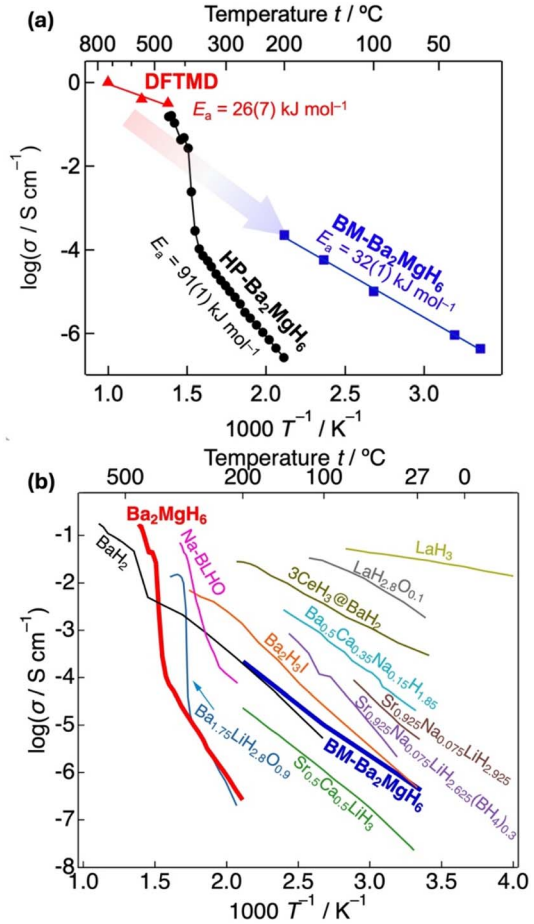

Fig. 8 (a) Arrhenius plot of the ball-milled (BM) and high-pressure (HP) samples of Ba_2MgH_6. (b) Conductivity comparison of previously reported typical hydride-ion conductors. Na-BLHO represents $Ba_{1.60}Li_{0.6}Na_{0.4}H_{2.25}O_{0.959}$.[2,8,9,11–15,38,39]

hydride-ion conductivity. Furthermore, the hydride-ion conductivity of BM- Ba_2MgH_6 from 473 K to room temperature exceeds that of the benchmark material BaH_2 and the perovskite-related material $Ba_{1.60}Li_{0.6}Na_{0.4}H_{2.25}O_{0.959}$, and is comparable to that of Ba_2H_3I at room temperature.[2,8,39] Although the conductivity remains lower than that of recently reported fluorite-type LnH_x and anti-AgI-type $Ba_{0.5}Ca_{0.35}Na_{0.15}H_{1.85}$,[9,11,12,35] it is noteworthy that this study introduces a new framework structure for hydride-ion conduction. While previously reported H^- conductors have predominantly employed well-established framework structures such as fluorite-type, perovskite-type, and anti-AgI-type structures, the cryptohalite-type Ba_2MgH_6 provides new guidelines for the rational design of hydride-ion conductors as well as other anion conductors such as F^-, Cl^-, and O^{2-}.

Conclusions

The cryptohalite-type Ba_2MgH_6 demonstrated excellent conductivity (0.125 S cm^{-1}) at 693 K with a distinct conductivity jump near 635 K owing to the formation of a superionic phase. The DC measurements and the observed isotope effect of conductivity during H/D exchange confirmed that hydride ions were the prominent carriers. In a structure with isolated MgH_6, the hydrogen would be immobile. However, introducing a Schottky defect in Ba_2MgH_6 facilitated hydride migration through hydrogen vacancies, as confirmed by the MD simulation and NEB calculations. The mechanochemical synthesis was shown to increase the ionic conductivity of Ba_2MgH_6. Further investigation on the details of how to introduce extrinsic Schottky defects to stabilize the superionic phase at lower temperatures is still needed. The Schottky defect-induced hydride superionic conductivity in Ba_2MgH_6 demonstrates that the cryptohalite-type structure serves as a new framework for H^- conduction, providing guidelines for the rational design of hydride-ion conductors as well as other anion conductors such as F^-, Cl^-, and O^{2-}.

Author contributions

R. K. designed and directed the project. Y. T. and G. J. worked on material synthesis. G. J., Y. T., and N. I. P. A. conducted electrochemical measurements and analysis. N. M. and N. I. P. A. conducted the first-principles calculations. N. M., T. M., Y. T., and N.I. P. A. discussed the data interpretation. N. I. P. A. wrote the manuscript in consultation with N. M., T. M., Y. T., K. S., and R. K. All authors discussed the results and contributed to the final manuscript.

Conflicts of interest

There are no conflicts to declare.

Data availability

All data supporting the findings of this study are available within the article and its supplementary information (SI) file. Supplementary information: additional electrochemical data, structural refinement and phase analysis from SXRD and Rietveld refinement, and computational results including density of states supporting the conduction mechanism. See DOI: https://doi.org/10.1039/d5ta09966h.

Acknowledgements

This study was supported by JSPS KAKENHI (No. 17H06145 and 19H05793) and PUTI-UI (No. PKS-217/UN2.RST/HKP.05.00/2025). Temperature-dependent SXRD experiments were performed at SPring-8 under Proposal No. 2019A1775. The computing resources of the TSUBAME3.0 supercomputer at the Tokyo Institute of Technology were used.

References

1 C. Messer, *J. Solid State Chem.*, 1970, **2**, 144–155.
2 M. C. Verbraeken, C. Cheung, E. Suard and J. T. S. Irvine, *Nat. Mater.*, 2015, **14**, 95–100.

3 N. Matsui, Y. Hinuma, Y. Iwasaki, K. Suzuki, J. Guangzhong, H. Nawaz, Y. Imai, M. Yonemura, M. Hirayama, G. Kobayashi and R. Kanno, *J. Mater. Chem. A*, 2020, **8**, 24685–24694.
4 G. Kobayashi, Y. Hinuma, S. Matsuoka, A. Watanabe, M. Iqbal, M. Hirayama, M. Yonemura, T. Kamiyama, I. Tanaka and R. Kanno, *Science*, 2016, **351**, 1314–1317.
5 Y. Iwasaki, N. Matsui, K. Suzuki, Y. Hinuma, M. Yonemura, G. Kobayashi, M. Hirayama, I. Tanaka and R. Kanno, *J. Mater. Chem. A*, 2018, **6**, 23457–23463.
6 F. Takeiri, A. Watanabe, A. Kuwabara, H. Nawaz, N. I. P. Ayu, M. Yonemura, R. Kanno and G. Kobayashi, *Inorg. Chem.*, 2019, **58**, 4431–4436.
7 H. Nawaz, F. Takeiri, A. Kuwabara, M. Yonemura and G. Kobayashi, *Chem. Commun.*, 2020, **56**, 10373–10376.
8 H. Ubukata, F. Takeiri, K. Shitara, C. Tassel, T. Saito, T. Kamiyama, T. Broux, A. Kuwabara, G. Kobayashi and H. Kageyama, *Sci. Adv.*, 2021, **7**, eabf7883.
9 T. Hirose, N. Matsui, T. Itoh, Y. Hinuma, K. Ikeda, K. Gotoh, G. Jiang, K. Suzuki, M. Hirayama and R. Kanno, *Science*, 2025, **389**, 1252–1255.
10 K. Fukui, S. Iimura, T. Tada, S. Fujitsu, M. Sasase, H. Tamatsukuri, T. Honda, K. Ikeda, T. Otomo and H. Hosono, *Nat. Commun.*, 2019, **10**, 2578.
11 K. Fukui, S. Iimura, A. Iskandarov, T. Tada and H. Hosono, *J. Am. Chem. Soc.*, 2022, **144**, 1523–1527.
12 W. Zhang, J. Cui, S. Wang, H. Cao, A. Wu, Y. Xia, Q. Jiang, J. Guo, T. He and P. Chen, *Nature*, 2023, **616**, 73–76.
13 T. Hirose, T. Mishina, N. Matsui, K. Suzuki, T. Saito, T. Kamiyama, M. Hirayama and R. Kanno, *ACS Appl. Energy Mater.*, 2022, **5**, 2968–2974.
14 T. Hirose, N. Matsui, K. Watanabe, T. Saito, K. Mori, K. Suzuki, M. Hirayama and R. Kanno, *Dalton Trans.*, 2025, **54**, 4180–4186.
15 M. A. Nowroozi, I. Mohammad, P. Molaiyan, K. Wissel, A. R. Munnangi and O. Clemens, *J. Mater. Chem. A*, 2021, **9**, 5980–6012.
16 S. Tachibana, C. Zhong, K. Ide, H. Yamasaki, T. Tojigamori, H. Miki, T. Saito, T. Kamiyama, K. Shimoda and Y. Orikasa, *Chem. Mater.*, 2023, **35**, 4235–4242.
17 N. Matsui, K. Mori, T. Saito, K. Noi, S. Fujinami, Y. Park, T. Tojigamori, K. Suzuki, T. Abe and R. Kanno, *Chem. Mater.*, 2025, **37**, 4798–4806.
18 T. Kim, T. Kim, T. Lee, Y.-E. Park, J. Kim, S. Kang, H. Kim, S. Hong, N. Matsui, H. Kim and S. Kim, *J. Am. Chem. Soc.*, 2025, **147**, 14244–14253.
19 S. Kawaguchi, M. Takemoto, K. Osaka, E. Nishibori, C. Moriyoshi, Y. Kubota, Y. Kuroiwa and K. Sugimoto, *Rev. Sci. Instrum.*, 2017, **88**, 085111.
20 R. Oishi, M. Yonemura, Y. Nishimaki, S. Torii, A. Hoshikawa, T. Ishigaki, T. Morishima, K. Mori and T. Kamiyama, *Nucl. Instrum. Methods Phys. Res., Sect. A*, 2009, **600**, 94–96.
21 R. Oishi-Tomiyasu, M. Yonemura, T. Morishima, A. Hoshikawa, S. Torii, T. Ishigaki and T. Kamiyama, *J. Appl. Crystallogr.*, 2012, **45**, 299–308.
22 K. Momma and F. Izumi, *J. Appl. Crystallogr.*, 2008, **41**, 653–658.
23 P. E. Blöchl, *Phys. Rev. B*, 1994, **50**, 17953–17979.
24 G. Kresse and D. Joubert, *Phys. Rev. B*, 1999, **59**, 1758–1775.
25 J. P. Perdew, A. Ruzsinszky, G. I. Csonka, O. A. Vydrov, G. E. Scuseria, L. A. Constantin, X. Zhou and K. Burke, *Phys. Rev. Lett.*, 2008, **100**, 136406.
26 G. Kresse and J. Hafner, *Phys. Rev. B*, 1993, **47**, 558–561.
27 G. Kresse and J. Furthmüller, *Phys. Rev. B*, 1996, **54**, 11169–11186.
28 G. Kresse and J. Furthmüller, *Comput. Mater. Sci.*, 1996, **6**, 15–50.
29 S. Nosé, *J. Chem. Phys.*, 1984, **81**, 511–519.
30 S. P. Ong, W. D. Richards, A. Jain, G. Hautier, M. Kocher, S. Cholia, D. Gunter, V. L. Chevrier, K. A. Persson and G. Ceder, *Comput. Mater. Sci.*, 2013, **68**, 314–319.
31 Z. Deng, Z. Zhu, I.-H. Chu and S. P. Ong, *Chem. Mater.*, 2017, **29**, 281–288.
32 K. Kadir and D. Noréus, *Z. Phys. Chem.*, 1993, **179**, 243–247.
33 F. Takeiri, A. Watanabe, K. Okamoto, D. Bresser, S. Lyonnard, B. Frick, A. Ali, Y. Imai, M. Nishikawa, M. Yonemura, T. Saito, K. Ikeda, T. Otomo, T. Kamiyama, R. Kanno and G. Kobayashi, *Nat. Mater.*, 2022, **21**, 325–330.
34 H. Mehrer, A. W. Imre and E. Tanguep-Nijokep, *J. Phys.: Conf. Ser.*, 2008, **106**, 012001.
35 N. Bonanos, A. Huijser and F. Poulsen, *Solid State Ionics*, 2015, **275**, 9–13.
36 K. Kato, K. Toyoura, A. Nakamura and K. Matsunaga, *Solid State Ionics*, 2014, **262**, 472–475.
37 T. Krauskopf, S. P. Culver and W. G. Zeier, *Inorg. Chem.*, 2018, **57**, 4739–4744.
38 J. Cui, R. Zou, W. Zhang, H. Wen, J. Liu, S. Wang, S. Liu, H. Chen, W. Liu, X. Ju, W. Wang, T. Gan, J. Li, J. Guo, T. He, H. Cao and P. Chen, *Nature*, 2025, **646**, 338–342.
39 K. Okamoto, F. Takeiri, Y. Imai, M. Yonemura, T. Saito, K. Ikeda, T. Otomo, T. Kamiyama and G. Kobayashi, *Advanced Science*, 2023, **10**, 2203541.